

Some Remarks on Basic Equations of Eulerian Approach in Icing Problems

*K. Tsuboi and **S. Kimura

*Dept. of Intelligent Systems Eng., Ibaraki University
4-12-1 Nakanarusawa, Hitachi, 316-8511, ktsuboi@mx.ibaraki.ac.jp
**Dept. of Mech. Eng., Kanagawa Institute of Technology
1030 Shimo-ogino Atsugi, 243-0292, skimura@me.kanagawa-it.ac.jp

Abstract— An attempt of Eulerian approach to icing problems is reported. The basic equations of water droplets dispersed in airflow and the computational procedure are described. Also, some technical difficulties concerning this attempt to icing problems are pointed out. Computational examples; these are local impingement efficiency along a stationary cylinder, water droplets distribution around an oscillating cylinder and simulated shape of hard-rime ice on an airfoil, show the effectiveness of this approach. Furthermore, recent results on mathematical features of the basic equations are mentioned, in which the behavior of the droplet density in small Stokes number is clarified. Based on the results, some essential remarks on Eulerian approach in icing problems are suggested.

I. INTRODUCTION

Ice accretion phenomena, which appear on the surface of structures in super-cooled fog, have been studied for long time [1]-[3]. In fact, we can take such examples of the phenomena in engineering fields as ice accretion on an airplane or a helicopter in flight and also on power lines in mountain areas and/or arctic regions.

Recently, knowledge on ice accretion phenomena has become more important for the security of natural disaster, the structural design of a construction and also the estimation of the performance of rotor blades for a helicopter or a wind turbine in cold climate regions. In particular, interaction between temporal change of ice shape and airflow is considered to play a serious role in the performance of blades in rotation [4].

In simulation of icing problems, Lagrangian approach is well known [1], [5]. In this way, airflow around an obstacle is obtained at first and then trajectories of droplets with inertia are calculated based on the field of airflow. We can estimate the time averaged mass flux of droplets on the surface from the trajectories, which gives "local impingement efficiency".

In Lagrangian approach, however, only the geometry of droplet trajectories are considered and motion of droplets along the trajectory is neglected. Therefore, it is not straightforward to extend this approach to unsteady problems.

On the other hand, it is possible to employ Eulerian approach in simulating icing problems. In this approach, a cloud of super-cooled water droplets dispersed in airflow is represented as continuum field quantities as well as the airflow. Flow of dispersed droplets is, then, described by the averaged velocity and density. Therefore, it is called 2-fluid model in

general. To extend this approach to unsteady problems is quite easy because the unsteady terms are already included in the basic equations.

It is true indeed that Eulerian approach is never novel in icing problems. In fact, some works were reported in 1980s, in which local impingement efficiency was estimated based on the same approach [6], [7]. In 1990s, simulated shapes with accreted ice have been obtained and the results have represented experimental data successfully [8]-[11].

In the present paper, we summarize the outline of Eulerian approach in icing problems and some computational results based on this approach are also presented, by which the effectiveness of this approach is demonstrated empirically. At the same time, we emphasize some remarks on the basic equations which relate to the droplet density.

II. SUMMARY OF EULERIAN APPROACH

A. Basic Equations

In natural wind, the amount of water included in unit volume of airflow, which is called Liquid Water Content (L.W.C.) [12], is rather small. In fact, it is known the value of L.W.C. is at most 1 g/m^3 . In this situation, it is considered that collision between dispersed water droplets is little important. Then, airflow including huge numbers of water droplets such as super-cooled fog can be modeled as 2-fluid description.

In the simplest description of this model, Stokes' law of fluid resistance between dispersed droplets and the carrier flow of air is considered. The governing equations for the dispersed phase of droplets are, then, given as follows.

$$\frac{\partial \eta}{\partial t} + \frac{\partial}{\partial x_j} (v_j \eta) = 0, \quad (1)$$

$$\frac{D}{Dt} (v_i) + \frac{1}{\tau} (v_i - U_i) = 0, \quad (2)$$

where v_i and U_i mean velocity vectors of the dispersed phase of droplets and the carrier phase of airflow, respectively. The quantity η indicates mass density of the dispersed droplets and the effect of mass change is neglected here for simplicity.

The parameter τ included in (2) is a coefficient of fluid resistance between a droplet and airflow and it physically means relaxation time of droplet motion. Since the diameter of dispersed water droplets in natural wind is ones to tens μm at

most, the relaxation time of droplet motion is estimated at the order of “*millisecond*” in general.

Non-dimensional form of the parameter τ is called (particle) Stokes number and defined in the following expression.

$$St = \tau \frac{U_\infty}{L}, \quad (3)$$

where U_∞ and L indicate reference velocity and length, respectively. In the case of $U_\infty = 10 \text{ m/s}$ and $L = 1 \text{ m}$, the value of Stokes number St is approximately of order 10^{-2} .

B. Procedure of Computation

In the present study, we employ finite difference method on body fitted coordinates system for solving the basic equations (1) and (2). Then, the procedure of computation in icing problems based on Eulerian approach is summarized as follows, which are all steps at one time marching procedure.

Step 1 Velocity field of airflow U_i is given according to a problem under consideration. For example, we take potential flows and incompressible viscous flows as the velocity field in the present paper.

Step 2 Equation (2) is solvable when relaxation time τ is defined according to the problem. Then, we can obtain the velocity field of the dispersed droplets v_i .

Step 3 The density distribution of the dispersed droplets η is determined passively from (1) with the velocity field v_i of step 2.

Step 4 From the density and incoming velocity of the dispersed water droplets along the body surface, we can calculate local impingement efficiency β defined in general as follows:

$$\beta = \eta_s v_s \Delta S, \quad (4)$$

where η_s and v_s indicate the droplets density and the incoming velocity on the surface, respectively. Also, ΔS is a small surface element.

Step 5 The accretion rate of ice w is calculated by the local impingement efficiency (4). In particular, when we consider hard-rime accretion, it is simply given as

$$w = \frac{\beta}{\rho_{ice} \Delta S}, \quad (5)$$

where ρ_{ice} means the density of accreted ice.

Step 6 Grid points on the body surface are moved with the velocity w in (5) and all grid points in computational domain are redistributed around an updated shape of accreted ice by using moving grid technique [9].

C. Modeling of Microscopic Behavior in Icing Process

In Eulerian approach, considering the averaged flow field of water droplets, the microscopic behavior of water droplets in accretion process on a body surface cannot be represented by the crude description. This means that some modeling of this process is necessary. Here, we consider two elementary processes; these are local impingement efficiency and growth direction of accreted ice.

Local impingement efficiency β in (4) is defined as the amount of water droplets incoming onto the body surface lo-

cally. It is, therefore, easy to understand that the quantity affects greatly the process of ice accretion. Then, we consider two different definitions of local impingement efficiency. One definition is based on the normal component of incoming velocity v_n at the surface, that is,

$$\beta_n = \eta_s v_n \Delta S. \quad (6)$$

The other is defined by using the x -component of incoming velocity v_x , which corresponds to uniform flow direction of airflow.

$$\beta_x = \eta_s v_x \Delta S. \quad (7)$$

Now, we also need to give a model for growing direction of the accreted ice. Here, two possibilities are considered simply; these are “normal” and “upwind” directions. The growth of “normal” or “upwind” direction means that accreted ice is assumed to be growing toward normal or upwind direction to the surface, respectively. The former possibility is quite standard in icing simulation while the latter comes from an observation of experimental results [4].

We have no information for determining these two processes unfortunately. Then, four possible assumptions of local impingement efficiency and growth direction of accreted ice are considered. The combination of the assumptions in each case is listed in Table I.

TABLE I
COMBINATION OF LOCAL IMPINGEMENT EFFICIENCY AND GROWTH DIRECTION OF ACCRETED ICE

No.	Definition of β	Growth direction
case 1	β_x	upwind
case 2	β_n	normal
case 3	β_x	normal
case 4	β_n	upwind

D. Remarks on Computational Technique

Here we describe two typical difficulties of computation in icing problems based on Eulerian approach and the treatment and/or improvement to them.

The first difficulty originates from the discrete representation of body shape with accreted ice. With growing the accreted ice, the length of contour around the ice shape increases inevitably. This situation makes the distance between the neighboring grid points larger and results in the deterioration of the accuracy representing the body shape.

In order to improve this difficulty, automated generation of grid point in computation is developed [9], in which a new grid point is generated on the portion of the accuracy deterioration and the physical quantities are given by the interpolation of the values on the originally neighboring grid points. This technique is performed in step 6 in the procedure of computation shown in section II-B.

The other difficulty is related to the characteristic time. When we treat icing problem as unsteady flow problem, there exist two different kinds of characteristic time; one comes

from unsteadiness of airflow and the other does from ice accretion rate. Unfortunately, time scale of these two physical processes is rather different.

We can easily estimate the ratio of these two characteristic times from (4) and (5). The following expression is considered.

$$\frac{w}{U_\infty} = \frac{\eta_s}{\rho_{ice}} \frac{v_s}{U_\infty} \sim O\left(\frac{\eta}{\rho_{ice}}\right), \quad (8)$$

where U_∞ is uniform velocity at upstream infinite.

Equation (8) suggests that the ratio of these characteristic times is determined from the density ratio between accreted ice and water droplets. When the values of 10^3 kg/m^3 and 1 g/m^3 (for example L.W.C.) are employed respectively, the ratio in (8) is estimated at $w/U_\infty \sim O(10^{-6})$. This means the unsteady icing problem is ‘‘stiff’’ problem and large numbers of steps for time marching is necessary to compute directly the problem.

Here, we look over a practical example of ice accretion on an airfoil, in which the reference length $L=120 \text{ mm}$ (the chord length of the airfoil) and uniform velocity $U_\infty=10 \text{ m/s}$. Then, the characteristic time of the unsteadiness is estimated at $L/U_\infty=0.012 \text{ s}$ while the time scale of ice accretion is ones to tens minutes from the experiment [4]. The ratio of ice accretion rate to characteristic velocity of airflow, therefore, approximately ranges over $10^{-4} \sim 10^{-5}$.

At the present stage, the efficient treatment of this difficulty is under investigation. We assume to set a larger value in the density ratio defined in (8) in order to prevent the increase of computational steps. However, this assumption can be interpreted as the artificial increase of L.W.C. and inevitably leads to the lack of sufficient relaxation time in motion of a water droplet.

III. COMPUTATIONAL EXAMPLES OF EULERIAN APPROACH

A. Local Impingement Efficiency of a Circular Cylinder

As the most fundamental example, computational results of local impingement efficiency around a stationary circular cylinder are presented. In this computation, steady potential flow is assumed as airflow velocity U_i in (2).

Two profiles of local impingement efficiency β_n and β_x on the cylinder surface in the case of $St=1.0$ are shown in Fig. 1, in which the origin of the abscissa corresponds to the front stagnation point of the cylinder. The broken line in each figure means local impingement efficiency of St infinite.

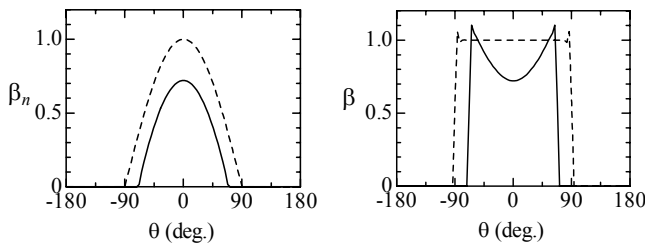


Fig. 1. Local impingement efficiency of a stationary circular cylinder in the case of $St=1.0$. Two profiles of β_n and β_x on the cylinder surface are shown in the left and right figures, respectively. The origin of the abscissa corresponds to the front stagnation point.

It is found that these two profiles are quite different. In fact, the distribution of β_n has one peak at the front stagnation while that of β_x has two peaks on the both sides of the stagnation. Although the former profile of β_n is typical result in Lagrangean approach, the latter of β_x is a distinctive result obtained by Eulerian approach.

B. Droplets Distribution around an Oscillating Cylinder

In order to simulate flow of droplets around an oscillating circular cylinder, we consider potential flow around a circular cylinder with the circulation in arbitrary motion in uniform flow [13]. The velocity potential is given as follows:

$$f(z) = z + \frac{1}{4} \frac{1}{z-\zeta} - \frac{1}{4} \frac{\dot{\zeta}}{z-\zeta} + \frac{\Gamma}{2\pi i} \log(z-\zeta), \quad (9)$$

where $z (=x+iy)$ and $\zeta (= \xi+i\eta)$ mean the coordinates of flow field and the center of the cylinder, respectively. The symbol Γ indicates the circulation of the cylinder. The third and fourth terms of (9), therefore, correspond to the effect of translating and rotational motions of the cylinder.

By using the circulation in (9), we present rotational motion of the cylinder in sinusoidal oscillation around the center. The circulation is given as

$$\zeta = 0, \quad \Gamma = \pi k_p \cos\left(\frac{k_p}{\gamma_p} t\right), \quad (10)$$

where k_p and γ_p are non-dimensional frequency and amplitude of the rotational angle.

On the other hand, translating motion of the cylinder perpendicular to uniform flow is, then, expressed according to the following way.

$$\zeta = i\eta \equiv i\gamma_h \sin\left(\frac{k_h}{\gamma_h} t\right), \quad \Gamma \equiv 0, \quad (11)$$

where k_h and γ_h mean non-dimensional frequency and amplitude of the translating motion.

Density distribution of water droplets around a cylinder in oscillation is depicted in Fig. 2; the result of rotational oscillation in the left figure and that of translating in the right, respectively. In the both figures, the blue colored region corresponds to low density of droplets and red does the high density. Also, we set $St=0.1$, $k_p=10.0$ and $\gamma_p=0.1$ (the amplitude is 10 deg.) in the computation of the rotational oscillation whereas $St=0.5$, $k_h=10.0$ and $\gamma_h=0.5$ (the amplitude is equal to the radius of the cylinder) are assumed in the case of translating oscillation.

Since the threshold of droplet collision on a cylinder St_{cr} is equal to $1/16$ ($=0.0625$), droplet impingement takes place when the cylinder is stationary under the condition of the rotational motion. However, oscillation of a cylinder in the period of the same order as the relaxation time of droplet motion prevents the collision on the cylinder surface and droplet free region forms around the cylinder.

In the case of translating motion, droplet impingement occurs on the upstream side of the cylinder since the value of St is beyond the threshold. On the other hand, the wake of droplet density with the width of the amplitude forms in the down-

stream side. This result means that water droplets in motion cannot follow the unsteadiness of airflow in the high frequency.

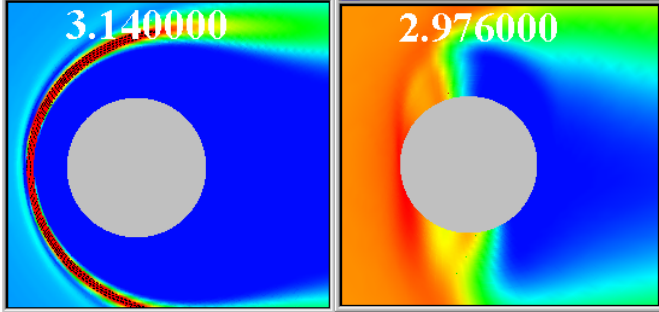


Fig. 2. Instantaneous density distribution of water droplets around an oscillating cylinder. The blue colored region corresponds to low density of droplets and red does the high density. Left figure for rotational oscillation around the center in $St = 0.1$, $k_p=10.0$ and $\gamma_p=0.1$ (the amplitude is 10 deg.). Right for translating oscillation perpendicular to uniform flow in $St = 0.5$, $k_h=10.0$ and $\gamma_h=0.5$ (the amplitude is equal to the radius).

C. Simulation of Accreted shape of Hard-rime Ice

As another example, we present computational results of hard-rime accretion on an airfoil because hard-rime accretion is considered as the simplest icing process, in which local impingement efficiency and growth direction of accreted ice play the most essential role.

In this simulation, viscous flow is employed as airflow in (2), which is calculated by unsteady incompressible Navier-Stokes equations. An airfoil of NACA0015 with the chord length 120 mm placed in airflow of the velocity 10 m/s at zero incidence is considered, which corresponds to Reynolds number $Re=10^5$ approximately. The averaged diameter of droplets is assumed to be 12 μm . Also, the density ratio in (8) is set to $\rho_{ice}/\eta = 100$ in the present simulation, which means the rate of ice accretion is assumed to be 10^4 times faster.

The simulated results of the length of accreted ice for each case of the assumption listed in Table I are shown in Fig. 3. The term “length of accreted ice” is defined as the length from the leading edge of the airfoil to the tip of accreted ice. Therefore, this figure shows the growth rate of the accreted ice.

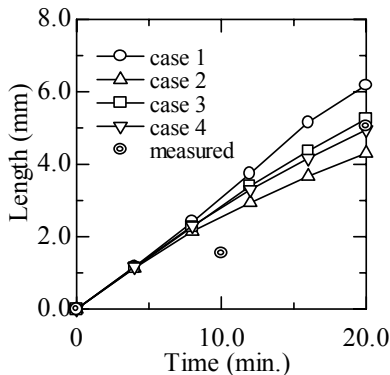


Fig. 3. Temporal development of the length of accreted ice. Growth rate of accreted hard-rime is rather different in each computational case (see Table I).

In this figure, we can find that the growth rate is rather different in each computational case. It is obvious that this fact originates in the definition of local impingement efficiency and growth direction of accreted ice. An experimental result is

also plotted in the same figure. Comparing the results of the computation with the experimental result, the results of case 3 and 4 show the good agreement with the experimental result.

Moreover, concerning the shape of accreted ice, we can summarize the characteristics as follows [9]:

Based on the definition of local impingement efficiency, we can classify the frontal part of ice shape into two types. In the case of β_n , the most ice-accreted portion appears at the leading edge and the ice becomes triangle shape toward the upstream direction. On the other hand, the shape is almost rectangular toward the upstream direction in the case of β_x . These features of the ice shape are, indeed, reflection of the profile of local impingement efficiency shown in Fig. 1.

The effect of growth direction of the accreted ice is observed in the upper and lower side of the ice shape. The accreted ice forms in the tapered shape toward the upstream direction in the case of growing to “upwind” direction while the shape of the upper and lower sides becomes approximately parallel to each other in the case of “normal” direction growth.

The simulated shapes of hard-rime ice in the case 3 are shown in Fig. 4 as an example. Each contour of the ice corresponds to the shape at every 200 s in actual time. It is found that the shape of ice is almost rectangle as mentioned above.

The results of the accretion rate and the ice shape lead to the conclusion that the assumption of case 3 can reproduce the experimental results of hard-rime accretion. This fact suggests that local impingement efficiency β_x , which is the distinctive result in Eulerian approach, works well in hard-rime accretion.

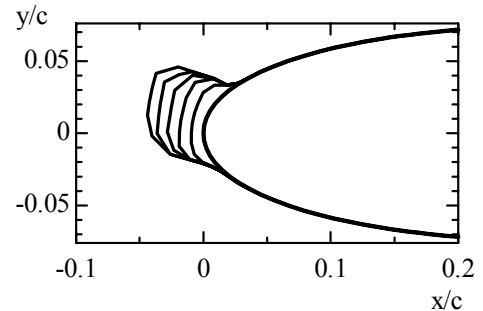


Fig. 4. An example of simulated shape of hard-rime accretion on an airfoil. Each contour of the ice corresponds to the shape at every 200 s in actual time. In this simulation, local impingement efficiency β_x and normal growth of ice are assumed.

IV. MATHEMATICAL FEATURES OF BASIC EQUATION

A. Inviscid Solution of Stagnation Region

We consider irrotational incompressible stagnation flow as a model of airflow, which is given as follows,

$$\begin{cases} U_1 = 2Ax_1, \\ U_2 = -\alpha Ax_2. \end{cases} \quad (12)$$

where A and α are constants, the values of which are summarized in Table II. Also, the value of St_{cr} means the threshold of droplet collision on the stagnation point.

It is noted that the negative value of A in (12) represents flow near the front stagnation while the flow simulates a separation region in the positive value.

TABLE II
 NUMERICAL VALUES OF CONSTANTS IN (12) FOR TYPICAL OBSTACLES.

Geometry	$ A $	α	St_{cr}
Cylinder	2	2	1/16
Plate	1	2	1/8
Sphere	3	1	1/24
Disc	$4/\pi$	1	$\pi/32$

When Stokes number St is smaller enough, no collision of droplets on a body surface occurs. Then, it is possible to obtain an exact solution, since the airflow field U_i is linear. Actually, we can find the following similar solution to the airflow,

$$\begin{cases} v_1 = f(St)U_1, \\ v_2 = g(St)U_2, \end{cases} \quad (13)$$

where $f(St)$ and $g(St)$ are functions of only St and these are given by

$$f(St) = \frac{-1 + \sqrt{1 + 8ASt}}{4ASt}, \quad g(St) = \frac{1 - \sqrt{1 - 4\alpha ASt}}{2\alpha ASt}.$$

It is notable that this solution holds in the following range of St and that the upper bound of the second condition corresponds to the threshold St_{cr} in Table II.

$$\begin{aligned} 0 \leq ASt \leq \frac{1}{4\alpha}, & \quad A > 0, \\ 0 \leq |A|St \leq \frac{1}{8}, & \quad A < 0. \end{aligned}$$

Now, droplets density can be obtained directly from the velocity field (13) and we have the solution

$$\eta = |x_1|^{g/f-1} F(|x_1|^{\alpha g} |x_2|^{2f}), \quad (14)$$

where F is an arbitrary function and keeps constant along the droplet trajectories.

Solution (14) suggests that the density field of droplets behaves along x_1 -axis as follows,

$$\begin{aligned} \eta &\sim |x_1|^{(\alpha+2)ASt}, & A > 0, \\ \eta &\sim \left(\frac{1}{|x_1|}\right)^{(\alpha+2)|A|St}, & A < 0, \end{aligned}$$

which mean that the singularity of x^{-St} appears in the droplet density near the stagnation while the density in separation point vanishes.

On the other hand, droplet collision occurs when St is beyond the threshold. In this region, the perturbed solution can be obtained. Then, we consider the velocity of airflow U_i by connecting the stagnation flow model (12) to uniform velocity at $x_1 = -1/(2|A|)$.

Based on the assumption of the airflow velocity, we have the following perturbed solutions.

0th order

$$v_1^{(0)} = 1, \quad v_2^{(0)} = 0, \quad \eta^{(0)} = 1$$

1st order

$$v_1^{(1)} = A(x_1 - \frac{1}{2A})^2, \quad v_2^{(1)} = -2A(x_1 - \frac{1}{2A})x_2, \quad \eta^{(1)} = 0$$

2nd order

$$\begin{aligned} v_1^{(2)} &= -\frac{A^2}{2}(x_1 - \frac{1}{2A})^3(x_1 + \frac{1}{6A}) \\ v_2^{(2)} &= -\frac{2}{3}A^2(x_1 - \frac{1}{2A})^2(x_1 - \frac{2}{A})x_2 \\ \eta^{(2)} &= \frac{2}{3}A^2(x_1 - \frac{1}{2A})^4 \end{aligned}$$

From these solutions, the density of droplet is given by the following series expression,

$$\eta = 1 + \frac{1}{St^2} \frac{2}{3} A^2 (x_1 - \frac{1}{2A})^4 + O(\frac{1}{St^3}). \quad (15)$$

The results of the droplet density in the vicinity of the stagnation for a stationary circular cylinder are summarized in Fig. 5 [14]. In this figure, the exact solution (14) in smaller St than the threshold and the perturbed solution (15) in large St are presented. At the same time, computational results in two different grid numbers are also plotted; the symbol \circ corresponds to the results with 100 by 70 grid points ($x_1 \sim 7 \times 10^{-4}$) and \square does the results with 200 by 200 grid points ($x_1 \sim 8 \times 10^{-5}$).

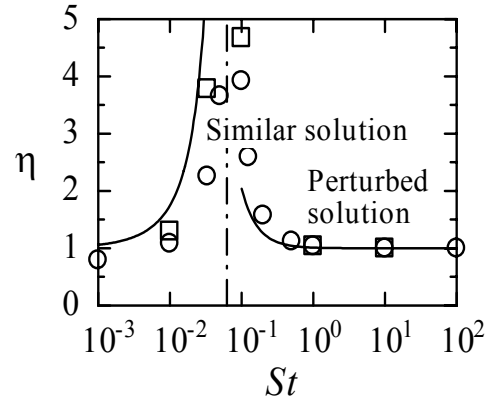


Fig. 5. Comparison of exact and perturbed solutions of the droplet density with computational results in the case of a circular cylinder. The symbol \circ corresponds to the results with 100 by 70 grid points and \square does the results with 200 by 200 grid points.

The qualitative agreement between the analytical solutions and the computational results is rather good despite of using the crude airflow velocity. Fig. 5 shows the droplet density has one peak at the threshold of St_{cr} ($=1/16$). Below the threshold, the density increases monotonously whereas above the threshold the density decreases sharply. Also, in the range of $St < St_{cr}$, the computed density is a little smaller than the exact value. This fact comes from the singularity of the solution (14) and suggests the possibility of underestimating the droplet density in the vicinity of the surface in simulation.

B. Droplet Free Layer and the Appearance Criteria

When $St < St_{cr}$, the solution of the droplet density (14) has the singularity along the surface. On the other hand, in the same range of St , it is known that a thin layer of droplet free appears along the surface, the thickness of which is of order St [15]. This fact means the singularity of droplets density vanishes in this thin layer. Therefore, the criteria for the appear-

ance of this droplet free layer gives important knowledge on the density field of droplets. Based on a simple order estimation of the basic equations, the criteria can be derived.

Now, we consider steady state of droplet flow field given by (1) and (2) where U_i is governed by incompressible Navier-Stokes equations. Under the assumption of small St , we have the following expressions as the first order approximation of St to the equations (1) and (2).

$$v_s \approx U_s + St \frac{\partial p}{\partial s} + O(St^2),$$

$$v_n \approx U_n + St \frac{\partial p}{\partial n} + O(St^2) \approx U_n + St \kappa U_s^2 + O(St^2),$$

where s and n indicate the local coordinates along the tangential and normal direction of the surface. Also, p is pressure field of airflow and κ means curvature of s -direction. The second term in the most right hand side of the normal component, therefore, gives the centrifugal force due to the tangential velocity U_s .

Assuming the boundary layer approximation for airflow velocity field, we obtain the following results [16].

(1) The droplet free layer appears along a surface and/or streamlines with curvature since the normal velocity due to the centrifugal force generates it.

(2) The droplet free layer appears when the following criteria are satisfied

$$\delta < \kappa St, \quad (16)$$

where δ is the thickness of viscous boundary layer of airflow.

The computational results on droplet free layer along a circular cylinder are shown in Fig. 6 in the case of $St=0.02$. In this figure, the thickness of the layer δ_p is depicted along the surface according to Reynolds number of airflow Re . The result of potential airflow is also included as $Re=\infty$.

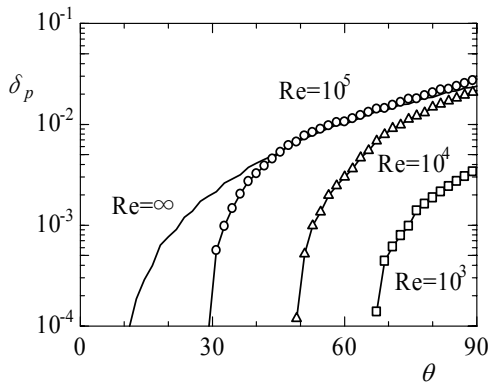


Fig. 6. Development of droplet free layer along a circular cylinder in the case of $St=0.02$. In these results, we estimate droplet density at free under the condition of $\eta \leq 10^{-3}$.

From this figure, we can find that the location at which droplet free layer appears, shifts to downstream direction with smaller Re and that the thickness of the layer in downstream region is independent from Re . Also, the droplet free layer does not appear at the front stagnation region even when Re is infinite. Since this layer generates by the centrifugal force acting on droplets, this result seems to be quite reasonable.

V. CONCLUDING REMARKS

We present the summary of Eulerian approach in icing problems, in which some technical difficulties are pointed out. Computational results of several problems are also shown and the effectiveness of this approach to icing problems is empirically demonstrated.

In particular, mathematical features of the basic equations obtained recently are described, which is related to the water droplet density. The droplet density in the vicinity of a body surface increases drastically when Stokes number is close to the threshold of droplet collision. This means careful treatment of the droplet density is necessary. Without it, the underestimation of local impingement efficiency may occur.

Furthermore, when Stokes number is smaller than the threshold, the density field of droplets is characterized by the singularity on the stagnation and droplet free layer along the downstream surface. Viscous effect of airflow delays the appearance of the droplet free layer and the singular region of droplet density increases with decreasing Reynolds number of airflow. Therefore, we need to pay our attention to the boundary condition of droplet density on the body surface in computations of small Stokes number.

VI. REFERENCES

- [1] I. Langmuir and K. B. Blodgett, "A mathematical investigation of water droplet trajectories", Tech. Rep. 5418, USAAF, 1946.
- [2] L. Makkonen, "Modeling of Ice Accretion on Wires", *J. Climate Appl. Meteor.*, vol. 23, pp. 929-939, 1984.
- [3] G. Poots, "Ice and snow accretion on structures", Research Studies Press, 1996.
- [4] S. Kimura, K. Tsuboi, S. Nishikawa and Y. Sugiyama, "The effect of airfoil motion on the shapes of ice accreted on an airfoil", *BOREAS IV in Hetta, Finland*, 1998.
- [5] K. J. Finstad and E. P. Lozowski, "A computational investigation of water droplet trajectories", *J. Atmos. Oceanic Tech.*, vol. 5, pp. 160-170, 1988.
- [6] P. McComber and G. Touzot, "Calculation of the Impingement of Cloud Droplets in a Cylinder by the Finite-Element Method", *J. Atmos. Sci.*, vol. 38, pp. 1027-1036, 1981.
- [7] J. N. Scott, W. L. Hankey, F. J. Giessler and T. P. Gelda, "Navier-Stokes Solution to the Flowfield Over Ice Accretion Shapes", *J. Aircraft*, vol. 25(8), pp. 710-716, 1988.
- [8] T. Hedde and D. Guffond, "ONERA Three-dimensional Icing Model", *AIAA J.*, 33(6), pp. 1038-1045, 1995.
- [9] K. Tsuboi and S. Kimura, "Numerical Simulation of Ice Accretion on a Body with Droplet Flow Model", *AIAA-99-3333*, pp. 1-7, 1999.
- [10] Y. Bourgault, W. G. Habashi, J. Dompierre and G. S. Baruzzi, "A finite element method study of Eulerian droplets impingement models", *Int. J. Numer. Meth. Fluids*, vol. 29, pp. 429-449, 1999.
- [11] G. F. Naterer, "Multiphase flow with impinging droplets and airstream interaction at a moving gas/solid interface", *Int. J. Multiphase Flow*, vol. 28, pp. 451-477, 2002.
- [12] L. Makkonen: "Analysis of Rotating Multicylinder Data in Measuring Cloud-Droplet Size and Liquid Water Content", *J. Atmos. and Ocean Tech.*, vol. 9, pp. 258-263, 1992.
- [13] K. Tsuboi and S. Kimura, "Computational Study on Local Impingement Efficiency of an Oscillating Circular Cylinder", *AIAA 2000-2661*, pp. 1-14, 2000.
- [14] K. Tsuboi, "Computational and analytical study on particle flow field around a circular cylinder", *AIAA paper 2001-2650*, pp. 1-9, 2001.
- [15] J. V. Healy, "Perturbed two-phase cylindrical type flows", *Phys. of Fluids*, vol. 13, pp. 551-557, 1970.
- [16] K. Tsuboi, "Computational investigation on flow field of particle phase in 2-fluid Saffman equation", *AIAA paper 2004-2647*, pp. 1-9, 2004.